The Astrophysical Journal, 889:175 (12pp), 2020 February 1 https://doi.org/10.3847/1538-4357/ab5aed

Dynamical Masses of Young Stars. II. Young Taurus Binaries Hubble 4, FF Tau, and HP Tau/G3

Aaron C. Rizzuto[1,4], Trent J. Dupuy[2], Michael J. Ireland[3], and Adam L. Kraus[1]
[1] Department of Astronomy, The University of Texas at Austin, Austin, TX 78712, USA
[2] Gemini Observatory, 670 N. Aohoku Place, Hilo, HI 96720, USA
[3] Research School of Astronomy & Astrophysics, Australian National University, Canberra, ACT 2611, Australia
Received 2018 February 9; revised 2019 November 4; accepted 2019 November 21; published 2020 February 4

Abstract

One of the most effective ways to test stellar evolutionary models is to measure dynamical masses for binary systems at a range of temperatures. In this paper, we present orbits of three young K+M binary systems in Taurus (Hubble 4, FF Tau, and HP Tau/G3) with very long baseline interferometry parallaxes. We obtained precision astrometry with Keck II/NIRC2, optical photometry with *Hubble Space Telescope*/Wide Field Camera 3, and low-resolution optical spectra with WIFeS on the ANU 2.3 m telescope. We fit orbital solutions and dynamical masses with uncertainties of 1%–5% for the three binary systems. The spectrum, photometry, and mass for Hubble 4 are inconsistent with a binary system, suggesting that it may be a triple system where the primary component consists of two stars. For HP Tau/G3 and FF Tau, model masses derived from spectral energy distribution-determined component temperatures and luminosities agree with the dynamical masses, with a small offset toward larger model masses. We find model ages for the primary components of these systems of ∼3 Myr, but find that the secondaries appear younger by a factor of two. These estimates also disagree with the age of the physically associated G-type star HP Tau/G2, which is older (∼5 Myr) according to the same models. This discrepancy is equivalent to a luminosity underprediction of 0.1–0.2 dex, or a temperature overprediction of 100–300 K, for K/M-type stars at a given model age. We interpret this as further evidence for a systematic error in pre-main-sequence evolutionary tracks for convective stars. Our results reinforce that the ages of young populations determined from the locus of M-type members on the HR diagram may require upward revision.

Unified Astronomy Thesaurus concepts: Binary stars (154); Fundamental parameters of stars (555); Interferometry (808); Pre-main sequence stars (1290); Star forming regions (1565)

1. Introduction

Age-dated stellar populations establish the timeline for the study of many different astrophysical processes, including disk evolution and dissipation (e.g., Rieke et al. 2005; Carpenter et al. 2006, 2009; Chen et al. 2011; Luhman & Mamajek 2012; Rizzuto et al. 2012), exoplanet formation and migration (e.g., Kraus & Ireland 2012; David et al. 2016; Donati et al. 2016; Mann et al. 2016a, 2016b), and stellar gyrochronology (e.g., Mamajek & Hillenbrand 2008; Douglas et al. 2016). In the absence of associated evolved high-mass stars to map the main-sequence turn-off, the descent of young low-mass stars onto the main sequence is the most sensitive tool available for dating a young ($\lesssim$20 Myr) association. For typical initial conditions, a solar-mass young star contracts to within 20% of its zero-age main sequence (ZAMS) over ∼30 Myr from an initial radius of more than twice its ZAMS radius—a difference in radius that is relatively easy to detect as an excess luminosity above the main sequence on a traditional HR diagram. This sensitivity does not necessarily translate to accuracy. There are theoretical suggestions (e.g., Baraffe et al. 2012) that there are a range of values for the internal stellar entropy at the conclusion of accretion, as well as a range in initial rotation rates (e.g., Mamajek & Hillenbrand 2008). However, observational evidence suggests that the majority of binary systems appear highly coeval (e.g., Kraus & Hillenbrand 2009), with only a small minority showing measurable age differences. Furthermore, in young groups containing early-type stars that have begun turning off the main sequence, HR diagram position does not accurately translate to age for convective stars with the current evolutionary models (e.g., Soderblom 2010; Kraus et al. 2015; Feiden 2016; Jeffries et al. 2017).

Multiple-star systems have been a key testing ground for pre-main sequence models (e.g., Simon et al. 2013; Schaefer et al. 2014, 2016; Montet et al. 2015; Nielsen et al. 2016). For the most part, stars in binary systems appear to be the same age, although a significant minority (∼1/3) of very young ($\lesssim$3 Myr) systems show significant age discrepancies between their components (e.g., Kraus & Hillenbrand 2009). Disentangling dispersion in initial conditions from uncertainties in evolutionary models and real age dispersion within a cluster requires additional data beyond temperature and luminosity. The most readily observable quantity is the dynamical mass, which can be observed through the orbits of binary stars (e.g., Boden et al. 2012; Dupuy & Liu 2017) or resolved line emission measurements of gaseous circumstellar disks (e.g., Simon et al. 2000; Czekala et al. 2016; Sheehan et al. 2019).

With the release of *Gaia* parallax measurements (Gaia Collaboration et al. 2018) for the majority of young (<20 Myr) G/K/M-type stars in the wider solar neighborhood (200 pc), we have begun obtaining high-angular resolution monitoring of a large sample of young binary systems in star-forming regions and young associations. This campaign will build a calibration sample for the next generation of models with dynamical mass measurements at the level of the expected *Gaia* parallax uncertainties (Rizzuto et al. 2016). These measurements will also allow interpretation of the *Gaia* photocenter motion data

[4] 51 Pegasi b Fellow.

for these young binaries, which will be contaminated by significant stellar variability (e.g., Rizzuto et al. 2017).

In this study, we present the orbits of three close binary systems in the Taurus-Auriga star-forming region discovered during the survey of Kraus et al. (2011), which have parallaxes measured with very long baseline interferometry (VLBI) or are associated with objects that have VLBI parallaxes. In Section 2 we describe the three Taurus binary systems, in Sections 3 and 4 we describe the NIRC2 aperture masking observations and orbit fits to the resulting astrometry, and in Sections 5 and 6 we describe the analysis of the *Hubble Space Telescope* (*HST*) photometry and Wide Field Spectrograph (WiFeS) spectra. In Section 7 we fit two-component spectral energy distributions (SEDs) to the binary systems to determine luminosities and temperatures, and then fit evolutionary models to the data. In Section 8 we discuss the performance of the models, and in Section 9 we discuss the implications of the results for the age of the Taurus population.

2. Taurus Binary Systems Sample

HP Tau/G3 was identified as a Taurus member by Cohen & Kuhi (1979) in a group of stars near HP Tau and has an integrated-light spectral type of M0.6 (Herczeg & Hillenbrand 2014). HP Tau/G3 was observed to be a a visual binary with contrast of $\Delta K = 1.5 \pm 0.1$ mag during the Keck non-redundant aperture masking survey of Kraus et al. (2011), though it had been resolved in earlier speckle imaging (R. White 2019, private communication). It is associated with and likely bound to HP Tau/G2, which has a VLBI parallax of 6.2 ± 0.03 mas (Torres et al. 2009). HP Tau/G3 was observed by *K2*, the repurposed *Kepler* mission, in campaign 13 (Howell et al. 2014). Inspection of the *K2* light curve rules out any eclipsing stellar companions.

FF Tau was first identified as a Taurus star by Jones & Herbig (1979), has an integrated-light spectral type of K8 (Herczeg & Hillenbrand 2015), and was identified as a binary system by Simon et al. (1987). Kraus et al. (2011) measured a contrast for the visual companion of $\Delta K = 1.04 \pm 0.02$ mag with non-redundant aperture mask interferometry. FF Tau was also observed by *K2*, ruling out additional eclipsing companions. Due to its close proximity on the sky ($\sim 7'$) it is highly likely that FF Tau belongs to the same physical association of stars as HP Tau, and thus has the same parallax as HP Tau/G2.

HP Tau/G2, HP Tau/G3, and FF Tau likely form a gravitationally bound system, with several other objects associated with this group. Indeed, within $7'$ one can find the Taurus systems HP Tau AB, KPNO Tau 15, HQ Tau, and Haro 6–28. These systems comprise $\sim$5% of the stellar mass of the northern part of the Tau-Aur association, but only $\sim 10^{-6}$ of the area. The alignment is therefore unlikely to be by chance, and we take all these objects to be associated. There is also no clear filamentary structure at the location of these systems in CO(1−0) maps of Taurus (Dame et al. 2001), adding weight to the idea that the objects are physically associated and not simply a filament seen in projection.

Investigation of the newly available *Gaia* DR2 (Gaia Collaboration et al. 2018) parallaxes for these systems supports this picture. With the exception of HP Tau, all of these system have parallaxes within 1σ of the VLBI parallax of HP Tau/G2 ($\omega = 6.2$ mas). HP Tau, which appears to be in the background with a parallax of 5.65 ± 0.11 mas was resolved with lunar occultation interferometry to be a binary system with separation of <20 mas (Richichi et al. 2005). The additional astrometric error term in *Gaia* DR2 is 0.46 mas, with a significance of 53σ, and the astrometric renormalized unit weight error is 1.33 (Lindegren et al. 2018), implying that the *Gaia* DR2 parallax is not reliable with only a five-parameter solution (Rizzuto et al. 2018).

Hubble 4 was first cataloged as a star thought to be associated with the reflection nebula near the highly extincted Herbig Be star V892 Tau (Hubble 1922), and was given a spectral type of K8.5 by Herczeg & Hillenbrand (2015). Hubble 4 was identified as a visual binary with contrast of $\Delta K = 0.39 \pm 0.01$ mag with Keck non-redundant masking by Kraus et al. (2011). It is relatively bright in the radio, and was observed with VLBI to have a distance of 132.8 ± 0.5 pc (Torres et al. 2007). Hubble 4 has also been extensively monitored with spectroscopy; Crockett et al. (2012) identified a 0.5–1.5 km s^{-1} RV variability on a period of $\sim$1.55 days that was determined to be spot-driven. The presence of further spectroscopic companions is unlikely given the lack of larger amplitude RV variability. Table 1 lists the basic properties of these three binary systems.

3. Keck NIRC2 Observations and Analysis

We have monitored the orbital motion of these three binary systems over the past 12 yr with the facility imager NIRC2 at the Keck II telescope, using non-redundant aperture masking interferometry (NRM) in the natural guide star AO mode. All NIRC2 AO images were taken with the smallest available pixel scale of 9.952 mas (Yelda et al. 2010) and the nine-hole aperture mask and multiple narrow-band IR filters. Each target was observed in one or both of the *K*-band filters K' (2.124 μm) and Kcont (2.27 μm), the CH_4S filter (1.5923 μm) and the Jcont filter (1.213 μm). Hubble 4 was also observed in the *Z* filter (1.0311 μm). We employed either a two-point or four-point dither pattern for each observation.

The aperture masking reduction used here was the same as that presented in Rizzuto et al. (2016) and Kraus et al. (2008), utilizing the complex triple-product, or closure-phase in addition to squared visibilities to remove uncommon path errors. A binary system model, consisting of a separation, position angle, and contrast, can then be fit to these observables to determine the relative astrometry and photometry at each epoch. A complete explanation of the reduction and closure-phase fitting method is given in the appendix of Kraus et al. (2008). Table 2 lists the details of the observations and the fitted astrometry and magnitude differences for the three binary systems.

4. Orbit Fitting and Dynamical System Masses

Orbital solutions were fit to the astrometric data for the three systems with a χ^2 minimization over a grid of orbital parameters. For each system, we first generated an initial sample of 10^4 semimajor-axis, eccentricity, and system mass trial values, spanning 0.5–1.5 times the maximum observed orbital separation and 0.1–2 $M_\odot$ in total system mass. We drew random masses rather than periods because spectral type information places useful constraints on the system masses and reduces the parameter space involved in the search. We then calculated orbital periods for each trial pair of system mass and semimajor-axis using Kepler's law. For each of the 10^4 random samples we then fit the remaining three orientation angles and

Table 1
Properties of the Three Taurus Binary Systems

2MASS	Name	R.A. (J2000)	Decl. (J2000)	SpT	r' (mag)	K (mag)	π (mas)
J04352089+2254242	FF Tau	04 35 20.90	+22 54 24.3	K8	13.1	8.59	(6.20 ± 0.03)
J04184703+2820073	Hubble 4	04 18 47.04	+28 20 07.3	K8.5	12.0	7.29	7.686 ± 0.032
J04355349+2254089	HP Tau/G3	04 35 53.50	+22 54 09.0	M0.6	⋯	8.80	(6.20 ± 0.03)
J04355415+2254134	HP Tau/G2	04 35 54.15	+22 54 13.6	G2	10.6	7.23	6.20 ± 0.03

Note. Spectral types are taken from Herczeg & Hillenbrand (2014), r' and K band magnitudes are taken from APASS (Henden et al. 2012) and 2MASS (Skrutskie et al. 2006) with typical uncertainties of 0.1 and 0.02 mag, respectively. System parallaxes are from the VLBI observations of Torres et al. (2007, 2009) for HP Tau/G3 and FF Tau, and from the latest observations of Galli et al. (2018). The parallaxes for FF Tau and HP Tau/G3 are given in parentheses because we are adopting the parallaxes measurement from the associated and bound star HP Tau/G2.

periastron times using a Levenberg–Marquardt least-squares regression. The χ^2 values for the trials were then inspected in the different orbital parameters to ensure no obvious bimodality in possible orbits was present. For all three systems, the observations spanned the majority of the full orbit, thus the orbital solutions were tightly constrained and the trail semimajor axis range used was significantly larger than the region of parameter space with allowed solutions. We then further restricted the range of trial parameters and drew a new random sample for which the process was repeated. The orbit parameters with the smallest reduced χ^2 value from this second sample were then taken as the starting point for a full fit over all seven orbital parameters using a Markov Chain Monte Carlo (MCMC) method. We used Foreman-Mackey et al. (2013) implementation of the Affine-invariant MCMC, using 20 walkers initialized randomly over parameter space spanned by $\Delta\chi^2 = 3$ from the initial search range. We sampled the posterior 30,000 times, with a 15,000 step burn-in, and calculated the 68% credible intervals. Combining our orbit solutions and the literature parallax measurements, we can estimate the dynamical system masses for the three binary systems. Table 3 lists the best-fit orbital parameters for the three systems and Figure 1 displays the orbital solutions.

5. *Hubble Space Telescope* Observations

In addition to AO imaging with Keck/NIRC2, we have also obtained single epoch observations of these binary systems with the *HST* Wide Field Camera 3 (WFC3), in a variety of visible filters spanning wavelengths of 200–1000 nm. Three exposures were taken in each filter, in the C512C subarray, and the standard *HST* reduction, calibration, and cosmic-ray rejection process was applied (Rajan 2010). We then performed simple aperture photometry on the drizzled *HST* images with a 0.″4 radius target aperture and a sky annulus of 4″–6″, and applied the standard WFC3 zero-point calibration to produce unresolved magnitudes for the systems. Table 4 lists the unresolved system magnitudes in the WFC3 filters, and Table 5 lists unresolved magnitudes from 2MASS and APASS (Skrutskie et al. 2006; Henden et al. 2012).

The epochs of the *HST* observations are within times spanned by the NRM orbit monitoring observations presented above, so the relative positions of the binary components are known to ∼1 mas for each system. The predicted astrometric uncertainties at the *HST* observation epoch are thus significantly smaller than the *HST*:WFC3 pixel scale (∼40 mas), and combined with the stability of the *HST* point-spread function (PSF) allow decomposition of the highly blended *HST*/WFC3 images to produce component contrast measurements in the optical bands for the Hubble 4 and HP Tau/G3 systems. FF Tau was found to be too close (<1 WFC3/UVIS pixel) at the time of *HST* observation for decomposition of the images.

Modeled after the work of Garcia et al. (2015) and our previous paper (Rizzuto et al. 2016), we first assembled a library of at least 50 PSFs in each filter in the C512C subarray on the UVIS2 detector from archival data with long exposures. We visually vetted individual PSF references for elongation due to binarity, blends, or nearby cosmic rays within a few pixels of the PSF center. Other contaminants were then handled with sigma clipping in the proceeding fits. Using the Tiny Tim software (Krist et al. 2011) we created PSF models for each WFC3 filter and fit these to the PSF reference library to determine a modified, super-sampled PSF model that most closely fits the library of PSF references.

We then fit the individual images for our binary systems using the new PSF models by sub-pixel shifting and adding the model PSF in each filter to create a model binary system with separation and position angle fixed by the orbit at the epoch of *HST* observation. Because many of the *HST* exposures were extremely short (<1 s) we expected some PSF blur induced by *HST*'s rotational shutter. This is a well-documented effect seen in exposures shorter than ∼5 s (Hartig 2008) and will directly affect the measured component contrasts. We model the shutter blur by applying a two-dimensional Gaussian blur to the model PSF in the binary fitting procedure, with extent in each axis and angle allowed to vary. Figure 2 displays an example fit to a single WFC3 image. Residuals for each image were typically ∼5% of the peak pixel value. Each object had three exposures in each WFC3 filter, and each of these images was fit separately, with different blur parameters and component contrasts. The contrasts and uncertainties were then combined with a mean to determine a final contrast ratio for the systems in each filter. Table 6 lists the contrasts for the Hubble 4 and HP Tau/G3 systems

6. WiFeS Observations

Low-resolution spectra of the three binary systems were obtained with the WiFeS on the Australian National University 2.3 m telescope (Dopita et al. 2007, 2010). WiFeS is a dual-beam, optical image-slicing spectrograph which provides low- to mid-resolution spectra over a contiguous 25″ by 38″ field of view, divided into 1 × 0.″5 spatial pixels. In the red arm, we used the R3000 grating, which provided spectral resolution of $R = 3000$ at wavelengths of 560–940 nm, and in the blue arm we used the B3000 grating, which provided spectral resolutions of $R = 3000$ down to 320 nm. Hubble 4 was observed on 2015 December 25, and HP Tau/G3 and FF Tau were observed on

Table 2
Table of Keck/NIRC2 Non-redundant Masking Observations

Epoch	MJD	Filter	Sep (mas)	P.A. (deg)	Contrast (mag)
			FF Tau		
2007 Nov 23	54427.579	K'	36.1 ± 0.4	356.4 ± 0.5	1.03 ± 0.02
2008 Dec 21	54821.520	K'	22.6 ± 2.2	342.0 ± 2.0	1.96 ± 0.36
2008 Dec 23	54823.463	CH_4S	20.8 ± 0.3	335.6 ± 0.3	1.28 ± 0.14
2010 Nov 29	55528.350	CH_4S	20.9 ± 0.3	152.0 ± 0.5	1.19 ± 0.06
2012 Jan 3	55929.475	CH_4S	23.5 ± 0.1	116.3 ± 0.1	1.21 ± 0.01
2012 Aug 12	56151.572	CH_4S	25.6 ± 0.2	98.6 ± 0.2	1.19 ± 0.02
2012 Dec 4	56265.420	CH_4S	26.7 ± 0.1	91.6 ± 0.2	1.23 ± 0.01
2013 Aug 7	56511.629	CH_4S	29.6 ± 0.3	77.3 ± 0.5	1.19 ± 0.02
2014 Aug 13	56882.584	CH_4S	34.7 ± 0.4	62.2 ± 0.5	1.19 ± 0.03
2014 Dec 9	57000.596	CH_4S	36.3 ± 0.3	58.0 ± 0.4	1.29 ± 0.02
2015 Dec 4	57360.235	K'	41.8 ± 0.3	48.4 ± 0.4	1.07 ± 0.02
2015 Dec 4	57360.530	Jc	41.3 ± 0.3	47.0 ± 0.4	1.13 ± 0.03
			HP Tau/G3		
2007 Nov 23	54427.583	K'	29.3 ± 1.6	91.8 ± 1.4	1.29 ± 0.18
2008 Dec 21	54821.525	K'	26.6 ± 0.8	130.6 ± 0.8	1.56 ± 0.10
2009 Nov 20	55155.478	Kc	22.4 ± 0.9	163.1 ± 2.1	1.39 ± 0.17
2010 Nov 28	55528.352	CH_4S	26.8 ± 1.7	216.7 ± 1.7	1.58 ± 0.11
2012 Jan 3	55929.235	CH_4S	35.7 ± 0.2	244.1 ± 0.2	1.60 ± 0.01
2012 Aug 12	56151.586	CH_4S	42.4 ± 0.5	253.3 ± 0.6	1.59 ± 0.04
2013 Aug 7	56511.626	CH_4S	52.5 ± 0.3	264.7 ± 0.2	1.59 ± 0.02
2014 Aug 13	56882.644	CH_4S	61.2 ± 1.0	274.5 ± 0.7	1.76 ± 0.08
2015 Sec 4	57360.231	K'	67.7 ± 0.4	280.9 ± 0.3	1.60 ± 0.02
2015 Sec 4	57360.543	Jc	68.7 ± 0.6	281.2 ± 0.5	1.59 ± 0.07
2018 Oct 31	58423.829	K'	81.1 ± 0.3	293.9 ± 0.2	1.53 ± 0.02
			Hubble 4		
2007 Nov 23	54427.530	K'	28.4 ± 0.1	106.1 ± 0.1	0.40 ± 0.01
2008 Dec 21	54821.505	K'	17.0 ± 0.6	284.3 ± 2.8	1.16 ± 0.34
2008 Dec 23	54823.442	CH_4S	17.9 ± 0.1	282.1 ± 0.4	0.60 ± 0.04
2008 Dec 24	54823.237	K'	16.5 ± 0.5	281.6 ± 2.1	0.70 ± 0.14
2009 Nov 20	55155.493	Kc	40.0 ± 0.1	228.1 ± 0.1	0.44 ± 0.01
2010 Nov 29	55528.283	K'	54.4 ± 0.1	207.0 ± 0.1	0.36 ± 0.01
2012 Jan 3	55929.228	CH_4S	63.2 ± 0.1	192.5 ± 0.1	0.39 ± 0.01
2012 Aug 12	56151.542	CH_4S	65.4 ± 0.1	185.9 ± 0.1	0.40 ± 0.01
2012 Dec 2	56263.555	CH_4S	66.4 ± 0.3	183.5 ± 0.4	0.35 ± 0.03
2013 Aug 6	56510.553	CH_4S	65.7 ± 0.1	175.7 ± 0.1	0.37 ± 0.01
2014 Aug 12	56881.643	CH_4S	61.9 ± 0.1	163.9 ± 0.1	0.39 ± 0.01
2015 Dec 4	57360.239	K'	49.7 ± 0.4	145.5 ± 0.5	0.34 ± 0.03
2015 Dec 4	57360.263	K'	49.5 ± 0.2	144.6 ± 0.1	0.39 ± 0.01
2015 Dec 4	57360.525	Jc	50.2 ± 0.2	145.2 ± 0.4	0.49 ± 0.03
2015 Dec 4	57360.329	Z	49.0 ± 0.6	143.7 ± 0.9	0.52 ± 0.07
2016 Nov 8	57700.495	CH_4S	35.08 ± 0.08	121.24 ± 0.16	0.38 ± 0.01

2015 December 27. The observations were taken in poor seeing, so the data in the blue arm of the spectrograph had low signal-to-noise ratios (S/Ns) (<10), as such we only report the red arm spectra here.

The WiFeS data were reduced using the PyWiFeS reduction packages[5] (Childress et al. 2014). PyWiFes transforms the CCD image, consisting of a linear spectrum for each spatial pixel, into a data cube. This includes bias subtraction, flat-fielding, bad pixel and cosmic-ray removal, sky subtraction, wavelength calibration, and flux calibration. The data are then interpolated to produce a consistent wavelength scale across each image pixel. We observed a flux calibrator from Bessell (1999) on each of the two observing nights, which were used for flux calibration of the target spectra. This process gives a single cube for each object, with dimensions $25'' \times 38'' \times 3650$ wavelength units. Following this reduction, we then applied the image combining method from Rizzuto et al. (2015), which fits a 2D-Moffat profile and background flux term to the image at each wavelength slice of the data cube and integrates the full target star flux at each wavelength to produce a linear spectrum. The resulting spectra for our targets had $S/N = 40-80$ over the wavelength range. Figure 6 displays the WiFeS spectra of the binary systems.

7. Two-component SED Fitting

Given the resolved and unresolved photometry for the binary systems we have obtained from a combination of WFC3 imaging (Table 6), NIRC2 non-redundant masking observations (Table 7),

[5] http://www.mso.anu.edu.au/pywifes

Table 3
Orbital Fits for FF Tau, HP Tau/G3, and Hubble 4

Name	T_0 (MJD)	P (days)	a (mas)	e	Ω (deg)	ω (deg)	i (deg)	$M_{\rm tot}$ ($M_\odot$)	χ^2_r
FF Tau	$55168.6^{+5.7}_{-5.6}$	$5393.5^{+66.8}_{-63.5}$	$38.85^{+0.49}_{-0.47}$	$0.634^{+0.004}_{-0.004}$	$176.8^{+0.4}_{-0.4}$	$305.2^{+0.3}_{-0.3}$	$124.9^{+0.5}_{-0.5}$	1.129 ± 0.027	3.2
HP Tau/G3	54804^{+28}_{-27}	9984^{+494}_{-436}	$56.35^{+0.94}_{-0.76}$	$0.521^{+0.009}_{-0.008}$	$292.5^{+1.5}_{-1.7}$	$200.8^{+5.0}_{-4.7}$	$45.7^{+1.2}_{-1.3}$	1.005 ± 0.053	3.4
Hubble 4	$54703.0^{+0.6}_{-0.7}$	$3392.0^{+1.3}_{-1.3}$	$41.64^{+0.06}_{-0.06}$	$0.68^{+0.001}_{-0.001}$	$65.7^{+0.8}_{-0.7}$	$68.4^{+0.7}_{-0.7}$	$159.2^{+0.3}_{-0.3}$	1.843 ± 0.024	4.4

and the low-resolution WiFeS spectra, it is possible to decompose the combined SED and spectrum of each binary into composite profiles and fit temperatures and luminosities for the components. We use unresolved photometry from WFC3 in the optical and 2MASS in IR. We exclude other catalog photometry to avoid complications due to stellar rotation, which is common at the 1%–10% level in the optical for young (<100 Myr) stars at the expected masses of these binary components (Rizzuto et al. 2017). The WFC3 data was taken in a single *HST* epoch, and the 2MASS IR data are significantly less contaminated by stellar variability at the longer wavelengths and as such we believe our data represents a best-case scenario for fitting SEDs to variable young stars where time variability in each measurement is not expected to be significant.

We use the BT-Settl atmosphere models in the fitting (Allard et al. 2011), with interpolation on the sparse grid of temperatures provided. Following this we convolve the models with filter profiles for the WFC3, 2MASS, and NIRC2 filters of interest to produce synthetic fluxes. We then convert the measured unresolved magnitudes from the WFC3 observations to flux measurements using the appropriate zero-points for the aperture size of 0.″4 used in the aperture photometry (Rajan 2010). We then also apply Gaussian instrumental broadening of $R = 3000$, and some minor rotational broadening of $20\,{\rm km\,s^{-1}}$ to the component model spectra for comparison to the WiFeS spectra.

We fit a six-component model to the resolved and unresolved photometry, consisting of two model temperatures, a radius ratio term, a reddening parameter, and an overall flux scale for both the photometry and the low-resolution spectrum. For the reddening, we interpolate the Savage & Mathis (1979) reddening law to each filter and apply it to the model photometry and component model spectra. We initially try a small grid of primary and secondary temperatures with starting points chosen based on the integrated-light spectral types and IR flux ratios, and then take the best grid-point as starting parameters for a Levenberg–Marquardt least-squares regression. We deliberately exclude any photometry blueward of the F555W filter, as the shorter wavelength filters are typically poorly fit by models for young stars. We also apply a 3σ clip to reject any additional photometry that is poorly fit by the models, this resulted in rejection of the F555W unresolved photometry for Hubble 4.

Figure 3 shows the final SED fits to the data for the three binary systems, including both the primary and the secondary component contributions to the total flux at each wavelength, and Figure 6 shows the model comparison to the WiFeS spectra. We then determine the component luminosities by integrating the model atmosphere fluxes at the best-fit temperatures according to the flux scale and ratio terms, and scaling by distance. Table 8 lists the best-fit temperatures, luminosities, and corresponding radii. We were unable to produce a two-component model that fit both the spectrum and the photometry for the Hubble 4 system: While the photometry alone is able to be fit with two components of temperature $T_{\rm eff} > 4100$ K, the WiFeS spectrum shows the characteristic TiO regions of a much lower temperature primary. We discuss this further below.

Following the SED fitting, we then compare the component temperatures and luminosities to evolutionary tracks from the BHAC models (Baraffe et al. 2015) to determine component ages and masses to compare to the total system masses from derived from the orbits. Figure 4 shows the HR diagram positions of the components of the three binary systems in relation to the 1–10 Myr BHAC (Baraffe et al. 2015), DSEP (Dotter et al. 2008) and PARSEC 1.2 s (Chen et al. 2014) isochrones and the corresponding total system masses compared to the dynamical masses. For all three models, the total system mass of HP Tau/G3 derived from the models is $\sim 1\sigma$ offset from the empirical values toward larger masses. FF Tau is also offset to higher model masses but by a smaller margin. Figure 5 shows the comparison of the dynamical system masses to the model-derived total system masses.

8. Model Comparison

The spectral types for these three binary systems were measured to be K7 (Kenyon & Hartmann 1995), and more recently updated to K8-M0.5 using optical spectra (Herczeg & Hillenbrand 2014). These spectral types imply somewhat cooler effective temperatures than what we find in the SED fitting. Veiling from accretion in the optical is unlikely to have introduced a significant spectral slope, as these stars do not have observable disk material. Indeed, Herczeg & Hillenbrand (2015) estimated that the effect of veiling in the optical for these systems was negligible. For the cases of FF Tau and HP Tau/G3, we expect that the combined light spectra, variable extinction in the Taurus clouds, and the steep age–mass gradient at this point on the pre-main sequence is the likely cause for the small difference in integrated-light spectral types and our two-component SED temperatures. For the Hubble 4 system, we discuss below that the data are most readily explained by the presence of a third, as yet unresolved, component to the system.

We also compared the best-fit two-component model spectrum for each binary system to the unresolved WiFeS spectra. The WiFeS spectra and model SED fit spectra are shown in Figure 6. The spectra for FF Tau and HP Tau/G3 both qualitatively match the two-component SED model in the 560–900 nm wavelength range, indicating the temperatures and reddening terms we infer from the resolved and unresolved photometry are consistent (Figure 6). The observed spectrum for Hubble 4 is significantly different from the SED model.

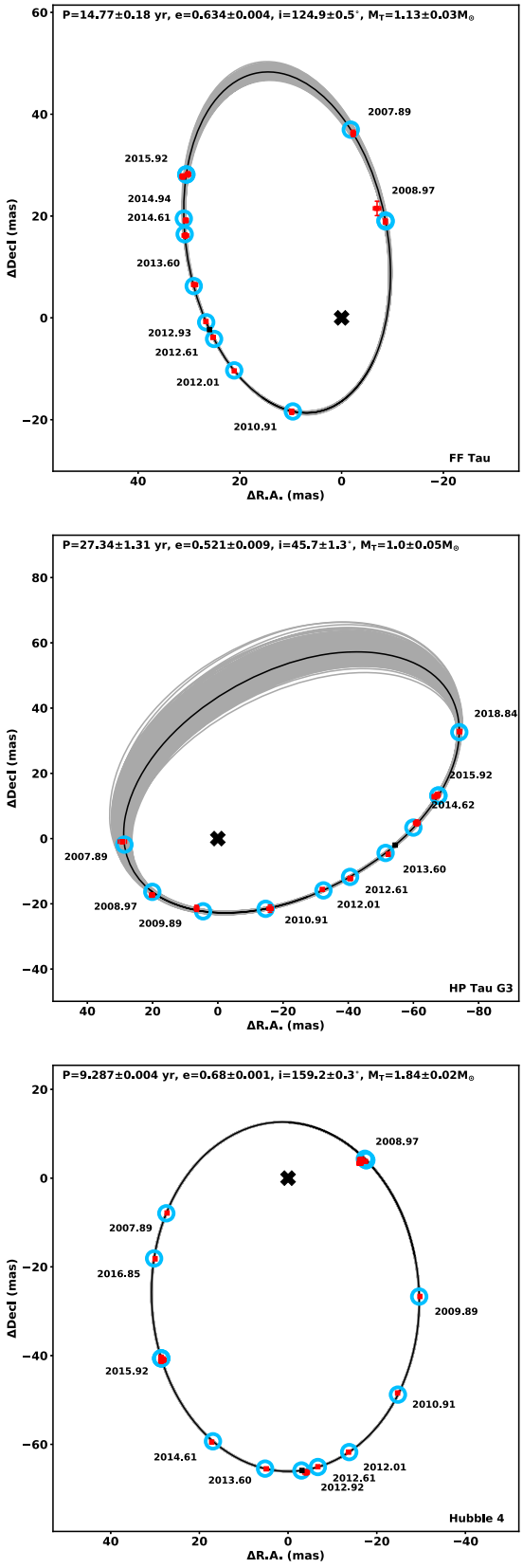

Figure 1. Orbital solution for FF Tau, HP Tau/G3, and Hubble 4. The black curve is the best-fit orbit, and the gray curves are 500 random orbits sampled from the fit posteriors. The red squares and blue circles indicate the observed astrometry and model predictions, respectively, and the black square indicates the orbital position of the secondary at the time of observation with *HST*.

Table 4
HST/WFC3 Unresolved Photometry

	FF Tau	HP Tau/G3	Hubble 4
Epoch	2012-10-14	2013-12-01	2012-11-28
F275W	20.38 ± 0.39	20.90 ± 0.59	17.61 ± 0.10
F336W	17.82 ± 0.07	18.85 ± 0.11	15.82 ± 0.03
F390W	16.78 ± 0.03	17.72 ± 0.04	15.16 ± 0.02
F395N	17.41 ± 0.08	18.25 ± 0.12	15.64 ± 0.04
F438W	15.91 ± 0.03	16.88 ± 0.03	14.46 ± 0.02
F475W	14.97 ± 0.02	15.83 ± 0.02	13.63 ± 0.02
F555W	14.02 ± 0.02	14.87 ± 0.02	12.82 ± 0.02
F625W	12.92 ± 0.02	13.66 ± 0.02	11.80 ± 0.02
F656N	12.06 ± 0.03	12.69 ± 0.04	10.84 ± 0.03
F775W	11.66 ± 0.02	12.24 ± 0.02	10.63 ± 0.02
F850LP	10.85 ± 0.02	11.28 ± 0.02	9.76 ± 0.02

Table 5
Unresolved Catalog Photometry

	FF Tau	HP Tau/G3	Hubble4
J	9.78 ± 0.02	10.04 ± 0.02	8.56 ± 0.02
H	8.93 ± 0.02	9.15 ± 0.02	7.64 ± 0.03
K	8.59 ± 0.02	8.80 ± 0.02	7.29 ± 0.02
B	15.84 ± 0.03	⋯	14.35 ± 0.08
V	13.87 ± 0.01	⋯	12.69 ± 0.05
g'	14.86 ± 0.01	⋯	13.51 ± 0.05
r'	13.07 ± 0.01	⋯	11.96 ± 0.04
i'	12.06 ± 0.01	⋯	10.96 ± 0.04

Note. J, H, and K magnitudes are taken from 2MASS (Skrutskie et al. 2006), and the optical magnitudes are taken from APASS (Henden et al. 2012).

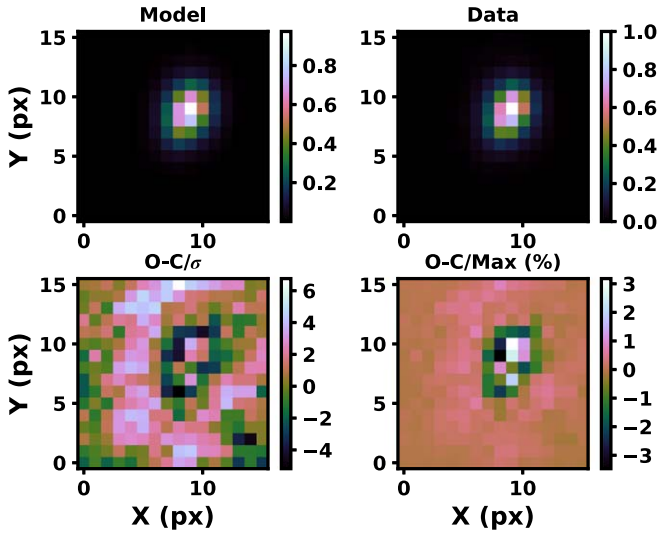

Figure 2. Example two-component PSF fitting to *HST*:WFC3 data for Hubble 4 in the F625W filter. The model PSF consists of two sources at the separation and position angle predicted by our orbital solutions, and a two-dimensional Gaussian blur. The resulting residuals are typically at the 1%–5% level.

8.1. Hubble 4

The TiO bands present in the WiFeS spectrum (Figure 6) indicate a cooler temperature for the components than what we infer from the unresolved photometry and magnitude differences. We note that the WiFeS spectrum implies a combined

Table 6
HST/WFC3 and NIRC2 Magnitude Differences for Hubble 4 and HP Tau/G3

Filter	Hubble 4	HP Tau/G3
F275W	0.78 ± 0.11	⋯
F336W	1.02 ± 0.05	⋯
F390W	0.96 ± 0.13	1.89 ± 0.81
F395N	0.88 ± 0.10	⋯
F438W	0.86 ± 0.14	3.84 ± 0.72
F475W	1.00 ± 0.11	..
F555W	0.99 ± 0.25	⋯
F625W	0.63 ± 0.12	3.41 ± 0.33
F656N	0.80 ± 0.15	2.20 ± 0.28
F775W	0.51 ± 0.26	2.56 ± 0.19
F850LP	0.66 ± 0.16	1.60 ± 0.15

Table 7
NIRC2 NIR Magnitude Differences

Filter	FF Tau	HP Tau/G3	Hubble 4
Δz	⋯	⋯	0.517 ± 0.068
ΔJc	1.132 ± 0.033	1.576 ± 0.064	0.486 ± 0.032
ΔCH_4S	1.219 ± 0.033	1.601 ± 0.028	0.378 ± 0.029
$\Delta K'$	1.052 ± 0.058	1.585 ± 0.106	0.382 ± 0.031
ΔKc	⋯	1.393 ± 0.166	0.440 ± 0.010

light spectral type of K7-M0, which is consistent with the temperature estimate of 3900 K from Herczeg & Hillenbrand (2015) and is significantly cooler than either of the components we fit to the Hubble 4 SED (Figure 3).

The discrepancy remains for Hubble 4 when considering the dynamical masses: it is difficult to reconcile the spectral type from the optical spectra with the dynamical system mass of $1.843 \pm 0.024\,M_{\odot}$ and the NIR secondary-to-primary flux ratio of ∼0.65. Galli et al. (2018) measured the component masses of the Hubble 4 system using VLBI, in combination with the orbit presented in this paper, and found the components to be $1.234 \pm 0.023\,M_{\odot}$ and $0.730 \pm 0.020\,M_{\odot}$ respectively. A $1.23\,M_{\odot}$ star at <5 Myr is expected to be significantly hotter that 3900 K according to multiple stellar evolution models (Dotter et al. 2008; Chen et al. 2014; Baraffe et al. 2015). We suggest that Hubble 4 may be a hierarchical triple system, with the primary consisting of two stars of unequal mass, with the effective temperature of the more massive component closer to ∼4000 K.

Given the extent and variety of the observations of the Hubble 4, there is only a small region of parameter space in which a third component to the system could exist. Inside the orbit of the known companion, observations using VLBI rule out additional stellar companions at angular separations >3 mas (Galli et al. 2018), and radial velocity monitoring rules out spectroscopic companions (Crockett et al. 2012). The only remaining possible configuration is a near face-on orbit ($i \simeq 0$) with separation <0.5 au. The secondary-to-primary mass ratio of the unresolved components must also be smaller than unity to produce the size and slope of the Hubble 4 A–B optical and NIR flux ratios. Such a companion may be detectable with additional VLBI monitoring if the posited component exhibits radio emission. Such a component may produce a orbital radial velocity signal smaller than the rotational variability-produced signal from Hubble 4 B, which would be expected to dominate if the two components of Hubble 4A are pole-on toward Earth.

8.2. HP Tau/G3 and FF Tau

For the two systems with mid-M secondaries, HP Tau/G3 and FF Tau, the PARSEC isochrones in both cases produce older ages by up to ∼2 Myr for the secondary components. The PARSEC evolutionary models employ the PHOENIX BT-Settl model atmospheres (Allard et al. 2011) for stars cooler than 4700 K, to produce the synthetic color–temperature/optical depth relations (Chen et al. 2014). This is then adjusted empirically to better match the colors of M-dwarf members of intermediate age clusters Praesepe and M67. It is unclear how this calibration to older M-dwarfs might affect our model fitting in the pre-main sequence for cooler stars. We expect that the systematic differences between the PARSEC models and the other two grids is produced by the calibration methodology.

The FF Tau and HP Tau/G3 primary components both have model-derived ages of ∼2.5–3.5 Myr, which is within the expected range for K-type stars in the Taurus clouds (Kraus et al. 2017). This age is in significant disagreement with the age of the nearby star HP Tau/G2. HP Tau/G2 is at the same distance and is associated with the both FF Tau and HP Tau/G3, and is likely bound to the latter. Kraus et al. (2011) surveyed HP Tau/G2 with NIRC2 coronagraphy and aperture masking, and did not find a nearby companion. HP Tau/G2 has a spectral type estimated from optical spectra of G2 (Herczeg & Hillenbrand 2014), which corresponds to a temperature of 5690 K according to their temperature scale and $\mathrm{Log}(L/L_{\odot}) = 0.84 \pm 0.10$ at the measured distance of the system of 161 pc (Torres et al. 2009). The Pecaut & Mamajek (2013) spectra-type to temperature conversion gives an effective temperature of 5870 K, which is in agreement with Herczeg & Hillenbrand (2014) within the uncertainties of the temperature scales. These values place HP Tau/G2 at a position on the HR diagram corresponding to an age closer to ∼5 Myr, (Figure 4), which is significantly older than the mean age of the three lower-mass binaries (∼2.5 Myr). This mass–age trend in the models extends to the companions to FF Tau and HP Tau/G3. In the comparison to both the DSEP and BHAC15 models, the model ages for the secondary components determined from temperatures and luminosities are systematically younger than the primaries by a factor of two.

The stellar membership of the Taurus-Auriga star-forming region is certainly not a coeval population. There are clear regions of ongoing stars formation surrounded by ∼1–3 Myr old pre-main sequence stars (Luhman et al. 2009), with spatial and kinematic subclustering (Luhman 2018; Galli et al. 2019). Additionally, the presence of a distributed, older, disk-free membership has been identified through spectral youth indicators with ages potentially as old as ∼20 Myr (Kraus et al. 2017), and confirmed with variability measurements with time-series photometry (e.g., David et al. 2019). It is thus possible that comparing two random Taurus stars may result in an age mismatch. This is unlikely to be the case for HP Tau/G2, HP Tau/G3, and FF Tau, which are likely coeval, potentially bound, and not associated with a deep column of gas or dust. Additionally, Galli et al. (2019) place these systems in a single Taurus subcluster. The discrepancies in age seen in this coeval test-case are largely mirrored for the wider Taurus population. Kraus & Hillenbrand (2009) find that HR diagram positions of single Taurus stars show a similar mass–age dependence between G and M-type stars.

The age difference between the G-type HP Tau/G2, the primaries of these binary systems, and the cooler secondaries is

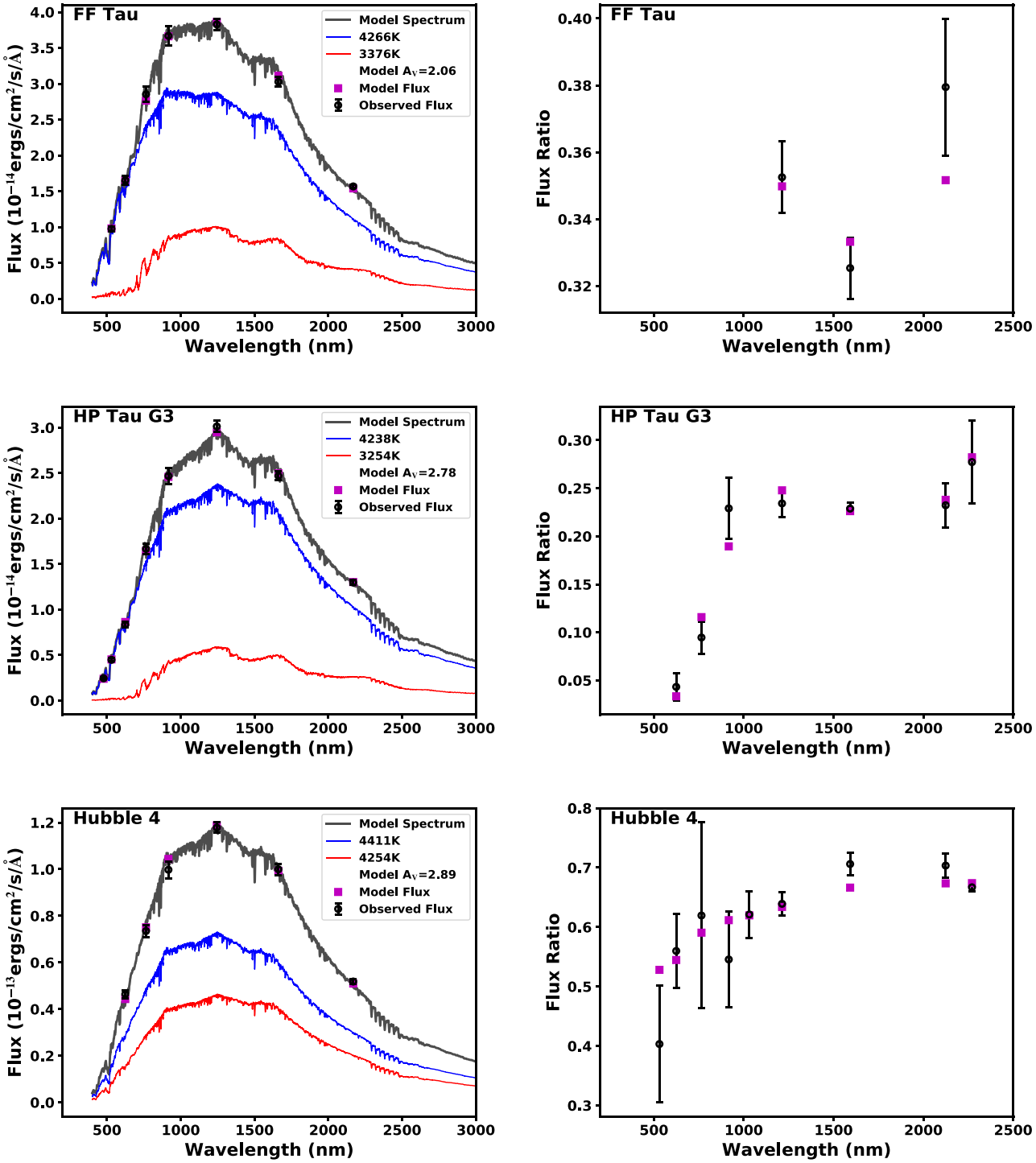

Figure 3. Two-component SED fits to the unresolved (left) and resolved (right) photometry for the three Taurus binaries in our orbit monitoring program. In the unresolved panels, the blue/red atmosphere profiles are the primary and secondary BT-Settl model atmospheres respectively, and the black profile is the combined model spectra. In all panels, black points with error bars are the measurements, and the purple squares are the forward-modeled photometry computed by integrating filter profiles on the model atmospheres and application of the best-fit extinction. Best-fit model parameters can be found in Table 8.

most likely the same model discrepancy in age as a function of stellar mass observed previously observed in young populations, including Taurus (Kraus & Hillenbrand 2009), the somewhat older 10 Myr population in Upper Scorpius (Preibisch et al. 2002; Pecaut et al. 2012; Rizzuto et al. 2016), and more distance clusters such as NGC 2264 (Park et al. 2000) and the Orion Nebula Cluster (Hillenbrand 1997), and is attributable to either a luminosity underestimation or temperature overestimation at a particular mass and pre-main sequence age in the model tracks. An underestimation of model luminosities at a given mass and age of 0.1–0.2 dex, or corresponding overestimation in model effective temperature of 100–300 K would account for the age difference between the three Taurus binary systems and HP Tau/G2. This is consistent with the discrepancies observed in the 10 Myr old Upper Scorpius population (Pecaut et al. 2012; Kraus et al. 2015;

Table 8
SED Fit Component Temperatures, Luminosities, Radii, and Reddening, and Corresponding Model Parameters for the Components of the Three Taurus Binary Systems

	FF Tau	HP Tau/G3	Hubble 4
$T_{\rm eff,p}$ (K)	4266 ± 124	4238 ± 75	4411 ± 164
$T_{\rm eff,s}$ (K)	3376 ± 160	3254 ± 100	4254 ± 156
L_p ($L_\odot$)	0.79 ± 0.10	0.78 ± 0.06	1.67 ± 0.26
L_s ($L_\odot$)	0.20 ± 0.04	0.14 ± 0.02	1.02 ± 0.16
R_p ($R_\odot$)	1.62 ± 0.14	1.64 ± 0.08	2.21 ± 0.24
R_s ($R_\odot$)	1.32 ± 0.20	1.16 ± 0.10	1.86 ± 0.20
$E(B-V)$ (mag)	0.66 ± 0.13	0.89 ± 0.05	0.93 ± 0.10
BHAC Fit Parameters			
Age$_p$ (Myr)	3.4 ± 1.3	3.2 ± 0.8	1.5 ± 0.8
Age$_s$ (Myr)	1.6 ± 0.7	1.9 ± 0.8	1.9 ± 0.8
M_p ($M_\odot$)	0.94 ± 0.14	0.9 ± 0.1	1.06 ± 0.2
M_s ($M_\odot$)	0.27 ± 0.08	0.22 ± 0.05	0.89 ± 0.2
$M_{\rm Tot}$ ($M_\odot$)	1.21 ± 0.22	1.12 ± 0.14	1.95 ± 0.4
DSEP Fit Parameters			
Age$_p$ (Myr)	3.1 ± 1.5	2.9 ± 0.9	1.1 ± 0.8
Age$_s$ (Myr)	1.5 ± 1.1	1.7 ± 0.7	1.7 ± 0.8
M_p ($M_\odot$)	0.92 ± 0.14	0.9 ± 0.1	0.95 ± 0.20
M_s ($M_\odot$)	0.29 ± 0.09	0.23 ± 0.05	0.85 ± 0.18
$M_{\rm Tot}$ ($M_\odot$)	1.22 ± 0.23	1.13 ± 0.13	1.8 ± 0.4
PARSEC Fit Parameters			
Age$_p$ (Myr)	2.5 ± 1.5	2.2 ± 0.9	1.1 ± 0.8
Age$_s$ (Myr)	3.5 ± 2.5	4.7 ± 1.5	1.5 ± 0.8
M_p ($M_\odot$)	0.80 ± 0.15	0.77 ± 0.08	0.88 ± 0.21
M_s ($M_\odot$)	0.46 ± 0.15	0.43 ± 0.09	0.76 ± 0.17
$M_{\rm Tot}$ ($M_\odot$)	1.26 ± 0.30	1.20 ± 0.17	1.65 ± 0.38

Note. Note that the parameters for Hubble 4 assume a two-component fit and ignore the discrepancy with the low-res spectra (see above).

Rizzuto et al. 2016), and also the older pre-main sequence field binary LSPM1314 (Dupuy et al. 2016).

9. Implications for the Age and Star Formation History of Taurus

There is evidence for a distributed population of slightly older (10–20 Myr) stars surrounding the Taurus clouds (e.g., Kraus et al. 2017) that formed in a previous epoch of star formation, much like the Sco-Cen-Ophiuchus complex in the south. The currently highly incomplete sample of this population suggests a very low disk fraction, implying that most of these objects have undergone disk dissipation. FF Tau, HP Tau/G3, Hubble 4, and HP Tau/G2 do not show evidence of a gaseous circumstellar disk in the near-IR or at 10–30 μm (Andrews & Williams 2005; Furlan et al. 2006; Luhman et al. 2006), though this is not particularly indicative of age. Binary systems undergo disk dissipation on a much shorter timescale than single stars (Kraus et al. 2012), so the lack of an observable IR excess for the three binary systems is not inconsistent with their youth. In the case of HP Tau/G2, because it is a G2-type star, it is not expected to still possess its primordial dust disk (Luhman et al. 2010). At 10 Myr, only ∼13% of G-type stars retain a debris disk (Carpenter et al. 2009), so the lack of a debris disk around HP Tau/G2 is again not indicative of age. The

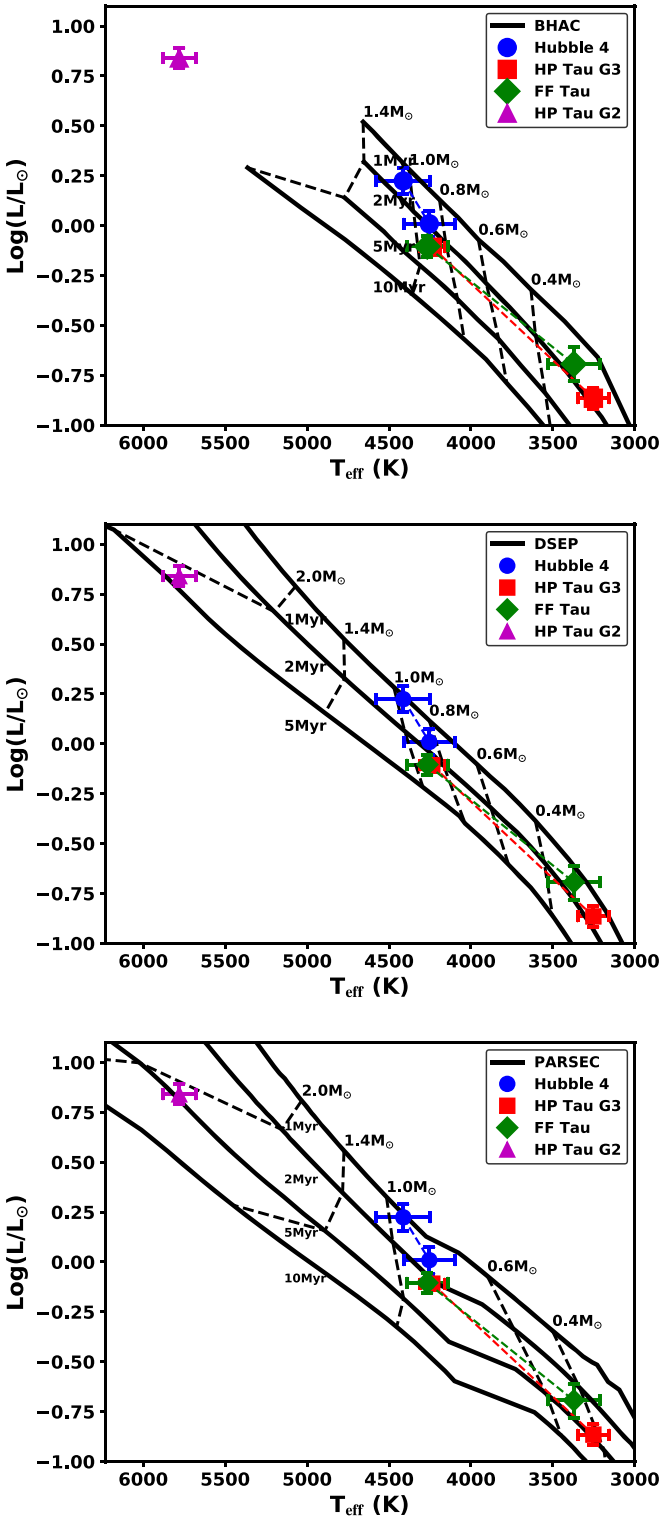

Figure 4. HR diagram positions for the components of the three binary systems derived from the luminosity and temperature and for the three pre-main sequence models, BHAC15 (Baraffe et al. 2015) (upper) DSEP (Dotter et al. 2008) (middle), and PARSEC 1.2 s (Chen et al. 2014) (lower). The binary system primary and secondary components are shown as colored points joined by lines. The black grid indicates the isochronal (solid) and isomass lines (dashed) for the each of the pre-main sequence models. We also show HP Tau/G2, a single G2-type star at the same distance as HP Tau/G3 and FF Tau, which appears to be significantly older compared to the model grids.

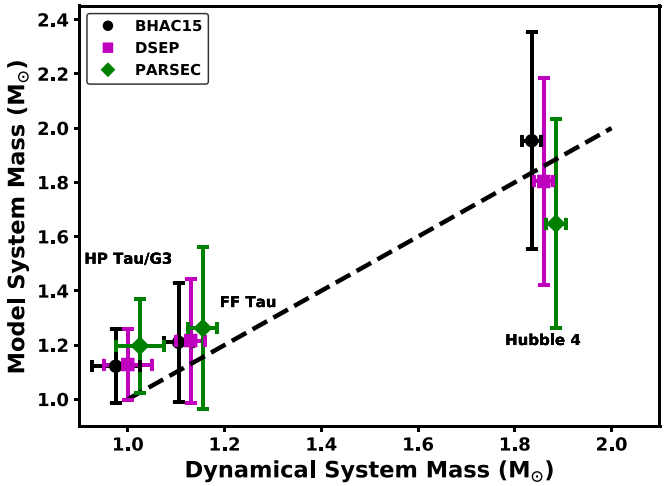

Figure 5. Comparison between the dynamical system masses and masses for the components of the binary systems computed from the SED fit temperatures and luminosities for the BHAC15 (Baraffe et al. 2015) (black circles), DSEP (Dotter et al. 2008) (purple squares), and PARSEC 1.2 s (Chen et al. 2014) (green diamonds) isochrones. The points are offset in dynamical mass for clarity. There is general agreement between the models and the mass measurements with a slight systematic offset to higher model temperatures for HP Tau/G3 and FF Tau. The SED fit temperature and luminosity uncertainties dominate the error budget, mainly due to the lack of precision-resolved photometry in the optical.

proximity of these systems to the molecular/dust clouds ($\sim$1° or $\sim$2–3 pc from cloud filament center), also implies they are likely not part of a distributed older population, but part of the classical Taurus membership.

There is now significant evidence that the current (and previous) generations of pre-main sequence evolutionary models (<20 Myr) underpredict the ages of convective M-type stars in associations of known age in comparison with higher-mass or earlier-type members (Pecaut et al. 2012; Kraus et al. 2015; Rizzuto et al. 2016; Jeffries et al. 2017). We have demonstrated above that the discrepancy extends to a bound and coeval Taurus multiple system (HP Tau/G2, HP Tau/G3AB, and FF TauAB). The classical age for Taurus is 0–2 Myr (Kraus & Hillenbrand 2009; Luhman et al. 2009), and is based on the HR diagram positions of the K/M-type population that make up most of the Taurus census. This potential systematic offset in low-mass model stellar ages suggests that Taurus may be older than the classical age, by up to a factor of two, though the introduction of additional physics like magnetic fields might be starting to resolve this discrepancy (e.g., Feiden 2016). This may also be the case for other star-forming regions age -dated solely on the basis of HR diagram positions of K/M-types stars using the current evolutionary models, and could further propagate to the inferred durations of earlier stages of protostellar collapse (Zacharias et al. 2013).

10. Summary

We have presented precise astrometric orbits and *HST* WFC3 photometry of three early K/M-type binary systems in the Taurus-Auriga star-forming region. Using the existing radio parallaxes for these systems, we determine system dynamical

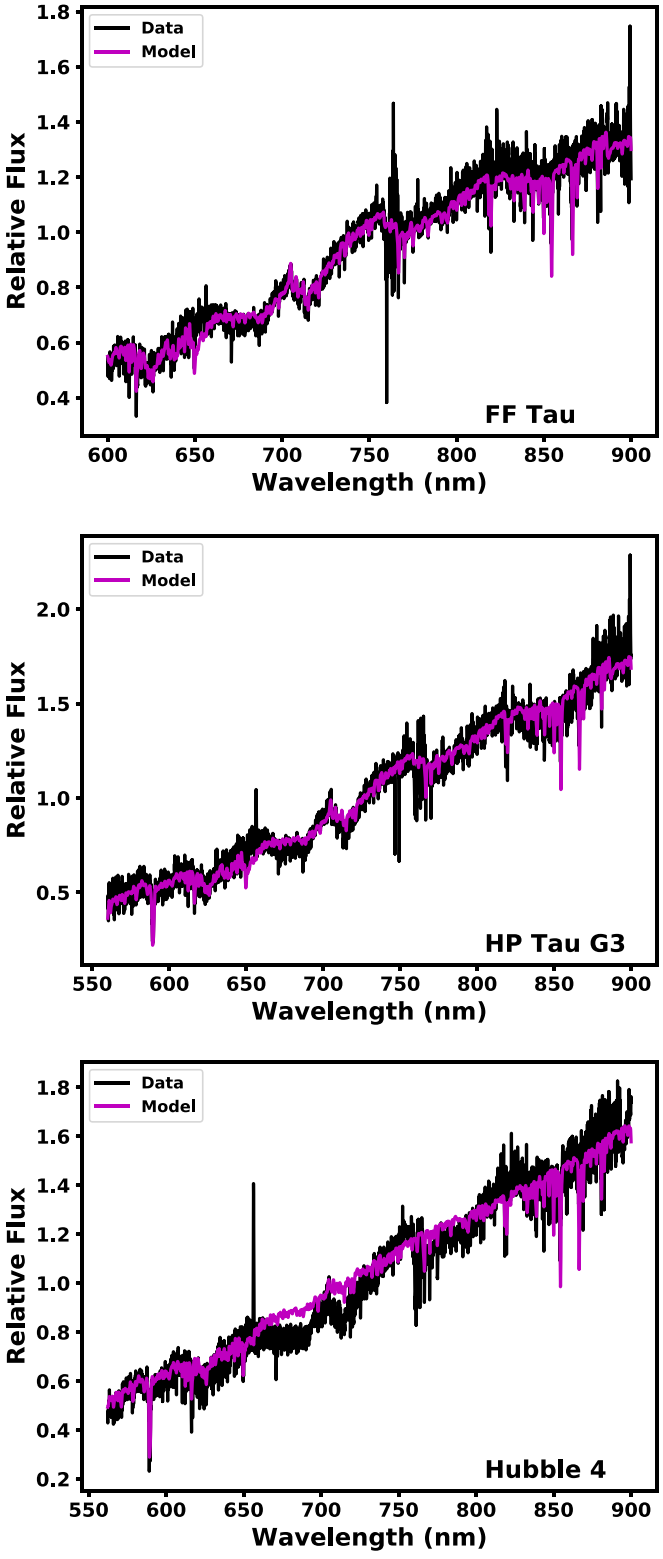

Figure 6. Sum of the two-component model spectra from the SED fitting compared to unresolved WiFeS spectra. The spectra for FF Tau and HP Tau/G3 match the SED fit profile relatively well, despite expected differences due to the youth of the sources. The unresolved spectrum of Hubble 4 is significantly different from the SED fit component temperature-combined spectrum. Given the NIR flux ratios observed in the orbit monitoring data and the component masses from Galli et al. (2018), we suggest that Hubble 4 may be a hierarchical triple system, with Hubble 4 A being an as yet unresolved binary system.

masses of ∼1%–5% for all three systems, and fit multi-band photometry and spectra to model atmospheres to determine component temperatures and luminosities. We then compared these observations to model evolutionary tracks to determine estimates of component masses and ages. In summary, we conclude that:

1. The model isochronal ages derived from comparison to evolutionary models (Dotter et al. 2008; Chen et al. 2014; Baraffe et al. 2015) for the three binary systems give ages in the range ∼1–3 Myr, which differs significantly from the age of the G2-type star HP Tau/G2, which is physically associated with HP Tau/G3 and FF Tau and thus provides a coeval test for the models.
2. The component model ages from temperatures and luminosities for the lower-mass companions to HP Tau/G3 and FF Tau are systematically younger than the corresponding primary components, suggesting a potential continuation of this trend to lower masses.
3. The model age discrepancy corresponds to the model luminosities being under-predicted by 0.1–0.2 dex, or the models temperatures being too hot by 100–300 K at a given pre-main sequence age and mass. This discrepancy is consistent with previous binary star results and pre-main sequence HR diagram age estimation trends with stellar mass for several young populations.

A.C.R. was supported as a 51 Pegasi b Fellow though the Heising-Simons Foundation. T.J.D. acknowledges research support from Gemini Observatory. Some of the data presented herein were obtained at the W. M. Keck Observatory, which is operated as a scientific partnership among the California Institute of Technology, the University of California and the National Aeronautics and Space Administration. The Observatory was made possible by the generous financial support of the W. M. Keck Foundation. The authors wish to recognize and acknowledge the very significant cultural role and reverence that the summit of Maunakea has always had within the indigenous Hawaiian community. We are most fortunate to have the opportunity to conduct observations from this mountain. This work was based on observations made with the NASA/ESA *Hubble Space Telescope*, obtained from the data archive at the Space Telescope Science Institute. STScI is operated by the Association of Universities for Research in Astronomy, Inc. under NASA contract NAS 5-26555. We also thank the anonymous referee for providing insightful and constructive comments.

ORCID iDs

Aaron C. Rizzuto https://orcid.org/0000-0001-9982-1332
Trent J. Dupuy https://orcid.org/0000-0001-9823-1445
Michael J. Ireland https://orcid.org/0000-0002-6194-043X
Adam L. Kraus https://orcid.org/0000-0001-9811-568X

References

Allard, F., Homeier, D., & Freytag, B. 2011, in ASP Conf. Ser. 448, 16th Cambridge Workshop on Cool Stars, Stellar Systems, and the Sun, ed. C. Johns-Krull, M. K. Browning, & A. A. West (San Francisco, CA: ASP), 91
Andrews, S. M., & Williams, J. P. 2005, ApJ, 631, 1134
Baraffe, I., Homeier, D., Allard, F., & Chabrier, G. 2015, A&A, 577, A42
Baraffe, I., Vorobyov, E., & Chabrier, G. 2012, ApJ, 756, 118
Bessell, M. S. 1999, PASP, 111, 1426
Boden, A. F., Torres, G., Duchêne, G., et al. 2012, ApJ, 747, 17
Carpenter, J. M., Mamajek, E. E., Hillenbrand, L. A., & Meyer, M. R. 2006, ApJL, 651, L49
Carpenter, J. M., Mamajek, E. E., Hillenbrand, L. A., & Meyer, M. R. 2009, ApJ, 705, 1646
Chen, C. H., Mamajek, E. E., Bitner, M. A., et al. 2011, ApJ, 738, 122
Chen, Y., Girardi, L., Bressan, A., et al. 2014, MNRAS, 444, 2525
Childress, M. J., Vogt, F. P. A., Nielsen, J., & Sharp, R. G. 2014, Ap&SS, 349, 617
Cohen, M., & Kuhi, L. V. 1979, ApJS, 41, 743
Crockett, C. J., Mahmud, N. I., Prato, L., et al. 2012, ApJ, 761, 164
Czekala, I., Andrews, S. M., Torres, G., et al. 2016, ApJ, 818, 156
Dame, T. M., Hartmann, D., & Thaddeus, P. 2001, ApJ, 547, 792
David, T. J., Cody, A. M., Hedges, C. L., et al. 2019, AJ, 158, 79
David, T. J., Hillenbrand, L. A., Petigura, E. A., et al. 2016, Natur, 534, 658
Donati, J. F., Moutou, C., Malo, L., et al. 2016, Natur, 534, 662
Dopita, M., Hart, J., McGregor, P., et al. 2007, Ap&SS, 310, 255
Dopita, M., Rhee, J., Farage, C., et al. 2010, Ap&SS, 327, 245
Dotter, A., Chaboyer, B., Jevremović, D., et al. 2008, ApJS, 178, 89
Douglas, S. T., Agüeros, M. A., Covey, K. R., et al. 2016, ApJ, 822, 47
Dupuy, T. J., Forbrich, J., Rizzuto, A., et al. 2016, ApJ, 827, 23
Dupuy, T. J., & Liu, M. C. 2017, ApJS, 231, 15
Feiden, G. A. 2016, A&A, 593, A99
Foreman-Mackey, D., Hogg, D. W., Lang, D., & Goodman, J. 2013, PASP, 125, 306
Furlan, E., Hartmann, L., Calvet, N., et al. 2006, ApJS, 165, 568
Gaia Collaboration, Brown, A. G. A., Vallenari, A., et al. 2018, A&A, 616, 1
Galli, P. A. B., Loinard, L., Bouy, H., et al. 2019, A&A, 630, A137
Galli, P. A. B., Loinard, L., Ortiz-Léon, G. N., et al. 2018, ApJ, 859, 33
Garcia, E. V., Dupuy, T. J., Allers, K. N., Liu, M. C., & Deacon, N. R. 2015, ApJ, 804, 65
Hartig, G. F. 2008, WFC3 UVIS Shutter Vibration-Induced Image Blur, Space Telescope Science Institute, Tech. Rep. WFC3 2008-44
Henden, A. A., Levine, S. E., Terrell, D., Smith, T. C., & Welch, D. 2012, JAVSO, 40, 430
Herczeg, G. J., & Hillenbrand, L. A. 2014, ApJ, 786, 97
Herczeg, G. J., & Hillenbrand, L. A. 2015, ApJ, 808, 23
Hillenbrand, L. A. 1997, AJ, 113, 1733
Howell, S. B., Sobeck, C., Haas, M., et al. 2014, PASP, 126, 398
Hubble, E. P. 1922, ApJ, 56, 162
Jeffries, R. D., Jackson, R. J., Franciosini, E., et al. 2017, MNRAS, 464, 1456
Jones, B. F., & Herbig, G. H. 1979, AJ, 84, 1872
Kenyon, S. J., & Hartmann, L. 1995, ApJS, 101, 117
Kraus, A. L., Cody, A. M., Covey, K. R., et al. 2015, ApJ, 807, 3
Kraus, A. L., Herczeg, G. J., Rizzuto, A. C., et al. 2017, ApJ, 838, 150
Kraus, A. L., & Hillenbrand, L. A. 2009, ApJ, 704, 531
Kraus, A. L., & Ireland, M. J. 2012, ApJ, 745, 5
Kraus, A. L., Ireland, M. J., Hillenbrand, L. A., & Martinache, F. 2012, ApJ, 745, 19
Kraus, A. L., Ireland, M. J., Martinache, F., & Hillenbrand, L. A. 2011, ApJ, 731, 8
Kraus, A. L., Ireland, M. J., Martinache, F., & Lloyd, J. P. 2008, ApJ, 679, 762
Krist, J. E., Hook, R. N., & Stoehr, F. 2011, Proc. SPIE, 8127, 81270J
Lindegren, L., Hernández, J., Bombrun, A., et al. 2018, A&A, 616, A2
Luhman, K. L. 2018, AJ, 156, 271
Luhman, K. L., Allen, P. R., Espaillat, C., Hartmann, L., & Calvet, N. 2010, ApJS, 186, 111
Luhman, K. L., & Mamajek, E. E. 2012, ApJ, 758, 31
Luhman, K. L., Mamajek, E. E., Allen, P. R., & Cruz, K. L. 2009, ApJ, 703, 399
Luhman, K. L., Whitney, B. A., Meade, M. R., et al. 2006, ApJ, 647, 1180
Mamajek, E. E., & Hillenbrand, L. A. 2008, ApJ, 687, 1264
Mann, A. W., Gaidos, E., Mace, G. N., et al. 2016a, ApJ, 818, 46
Mann, A. W., Newton, E. R., Rizzuto, A. C., et al. 2016b, AJ, 152, 61
Montet, B. T., Bowler, B. P., Shkolnik, E. L., et al. 2015, ApJL, 813, L11
Nielsen, E. L., De Rosa, R. J., Wang, J., et al. 2016, AJ, 152, 175
Park, B.-G., Sung, H., Bessell, M. S., & Kang, Y. H. 2000, AJ, 120, 894
Pecaut, M. J., & Mamajek, E. E. 2013, ApJS, 208, 9
Pecaut, M. J., Mamajek, E. E., & Bubar, E. J. 2012, ApJ, 746, 154
Preibisch, T., Brown, A. G. A., Bridges, T., Guenther, E., & Zinnecker, H. 2002, AJ, 124, 404
Rajan, A. E. 2010, WFC3 Data Handbook v. 2.1 (Baltimore, MD: STSci)
Richichi, A., Percheron, I., & Khristoforova, M. 2005, A&A, 431, 773

Rieke, G. H., Su, K. Y. L., Stansberry, J. A., et al. 2005, ApJ, 620, 1010
Rizzuto, A. C., Ireland, M. J., Dupuy, T. J., & Kraus, A. L. 2016, ApJ, 817, 164
Rizzuto, A. C., Ireland, M. J., & Kraus, A. L. 2015, MNRAS, 448, 2737
Rizzuto, A. C., Ireland, M. J., & Zucker, D. B. 2012, MNRAS, 421, L97
Rizzuto, A. C., Mann, A. W., Vanderburg, A., Kraus, A. L., & Covey, K. R. 2017, AJ, 154, 224
Rizzuto, A. C., Vanderburg, A., Mann, A. W., et al. 2018, AJ, 156, 195
Savage, B. D., & Mathis, J. S. 1979, ARA&A, 17, 73
Schaefer, G. H., Hummel, C. A., Gies, D. R., et al. 2016, AJ, 152, 213
Schaefer, G. H., Prato, L., Simon, M., & Patience, J. 2014, AJ, 147, 157
Sheehan, P. D., Wu, Y.-L., Eisner, J. A., & Tobin, J. J. 2019, ApJ, 874, 136
Simon, M., Dutrey, A., & Guilloteau, S. 2000, ApJ, 545, 1034
Simon, M., Howell, R. R., Longmore, A. J., et al. 1987, ApJ, 320, 344
Simon, M., Schaefer, G. H., Prato, L., et al. 2013, ApJ, 773, 28
Skrutskie, M. F., Cutri, R. M., Stiening, R., et al. 2006, AJ, 131, 1163
Soderblom, D. R. 2010, ARA&A, 48, 581
Torres, R. M., Loinard, L., Mioduszewski, A. J., & Rodríguez, L. F. 2007, ApJ, 671, 1813
Torres, R. M., Loinard, L., Mioduszewski, A. J., & Rodríguez, L. F. 2009, ApJ, 698, 242
Yelda, S., Lu, J. R., Ghez, A. M., et al. 2010, ApJ, 725, 331
Zacharias, N., Finch, C. T., Girard, T. M., et al. 2013, AJ, 145, 44